Journal of Zhejiang University-SCIENCE B (Biomedicine & Biotechnology) in press
www.jzus.zju.edu.cn; www.springer.com/journal/11585
E-mail: jzus_b@zju.edu.cn

Research Article

https://doi.org/10.1631/jzus.B2500462

SWCNTs/PEDOT:PSS-modified microelectrode arrays reveal striatal-hippocampal neural encoding of movement initiation and place fields during goal-directed navigation

Jin SHAN[1,2*], Wei XU[1,2*], Jinping LUO[1,2], Yaoyao LIU[1,2], Ming LI[1,2], Luyi JING[1,2], Yu WANG[1,2], Shiya LV[1,2], Zhaojie XU[1,2], Juntao LIU[1,2], Yiming DUAN[1,2], Qianli JIA[1,2], Yilin SONG[1,2✉], Mixia WANG[1,2✉], Xinxia CAI[1,2✉]

[1]*State Key Laboratory of Transducer Technology, Aerospace Information Research Institute, Chinese Academy of Sciences, Beijing 100190, China*
[2]*School of Electronic, Electrical and Communication Engineering, University of Chinese Academy of Sciences, Beijing 100049, China*

Abstract: Goal-directed navigation necessitates coordinated interactions among multiple brain regions, with the hippocampus and striatum playing critical roles in spatial representation, movement-related information, and reward-related evaluation. The hippocampus, particularly the CA1 (Cornu Ammonis 1) region, is renowned for its role in spatial encoding via place cells. The striatum, a basal ganglia nucleus, can integrate cortical, thalamic, and limbic inputs to regulate motor planning, reward valuation, and behavioral flexibility. Despite extensive research, a key challenge remains: the lack of high spatiotemporal resolution, high-precision, and multi-channel electrodes that are structurally matched for reliable implantation across multiple brain regions. To address this, we developed two silicon-based microelectrode arrays (MEAs) anatomically tailored for dual-region neuronal electrophysiological recording of the striatum and CA1. By modifying the electrode sites with SWCNTs/PEDOT:PSS nanocomposites, we significantly enhanced the electrical performance, reducing impedance and phase delay. Leveraging this platform, we demonstrated that neurons in the rat ventral striatum (vStr) contribute to movement initiation, transmitting information to CA1, while CA1 place cells dynamically encode new goal locations and relay spatial information to neurons in the dorsal striatum (dStr). This research provides a reliable platform for exploring the neural interactions between the striatum and hippocampus, establishing a foundation for future studies on neural circuits in complex behaviors.

Key words: Microelectrode array; SWCNTs/PEDOT:PSS; Electrophysiology; Navigation

1 Introduction

Goal-directed navigation is a complex cognitive process that integrates spatial mapping (Dupret et al., 2010), motivational drive (Syed et al., 2016), reward evaluation (Sosa et al., 2021), and target selection (Penner et al., 2012; Tryon et al., 2017) into cohesive behavior. Successful navigation requires animals to dynamically

✉ Xinxia CAI, xxcai@mail.ie.ac.cn
Yilin SONG, ylsong@mail.ie.ac.cn
Mixia WANG, wangmixia@mail.ie.ac.cn
* The two authors contributed equally to this work
Xinxia CAI, https://orcid.org/0000-0001-5997-7252
Yilin SONG, https://orcid.org/0000-0001-7756-5139
Mixia WANG, https://orcid.org/0000-0002-1310-8075
Jin SHAN, https://orcid.org/0000-0002-5409-1759
Wei XU, https://orcid.org/0000-0001-8884-0984

Received Aug. 3, 2025; Revision accepted Dec. 15, 2025
Crosschecked xxx. xx, 20xx; Published online xxx. xx, 20xx

encode environmental cues (place fields), initiate context-appropriate movements, and adjust strategies based on expected rewards. The hippocampal CA1 (Cornu Ammonis 1) region, via place cells, generates precise spatial representations and transmits contextual information, receiving inputs primarily from the entorhinal cortex, which encodes spatial and temporal information (Cholvin et al., 2021; Marks et al., 2021). The striatum receives environmental information from the cortex and engages in reciprocal communication with the thalamus, playing diverse roles in reward encoding, motor control, and habitual behavior (Cruz et al., 2023). Although the functions of both brain regions have been extensively studied, the temporal dynamics and coding principles governing striatal-hippocampal interactions during navigation remain unclear.

A critical barrier to dissecting these interactions lies in the limitations of conventional neural recording technologies. Traditional tungsten probe and other meta microelectrodes have been used widely in electrophysiological research owing mainly to their straightforward fabrication processes and well-established manufacturing protocols. However, their manufacturing process makes it challenging to scale up channel count and density. In contrast, silicon-based microelectrode arrays (MEAs) offer advantages including customizable shank geometries for anatomical targeting, multiple recording sites, and compatibility with integrated circuits (Zhang et al., 2016; Xu et al., 2024). However, bare electrodes typically exhibit suboptimal impedance (around 1 MΩ), which can lead to a high noise baseline and impair electrophysiological recordings (Cogan et al., 2008). Consequently, surface modification of electrode sites with conductive materials is essential to optimize the electrochemical performance and signal transduction efficiency of the electrodes. Metallic modifications, such as platinum nanoparticles and gold nanoparticles, can significantly reduce electrode site impedance (Zhang et al., 2016; Lee et al., 2018). In recent years, conductive polymers (CPs) have gained increasing attention for their excellent biocompatibility and good conductivity, making them increasingly used in bio-signal detection (Bettucci et al., 2022). Poly(3,4-ethylene dioxythiophene): poly(styrene sulfonate) (PEDOT:PSS) has gained popularity due to its excellent adhesion, biocompatibility, and stable conductivity (Kayser et al., 2019; Donahue et al., 2020; Huang et al., 2024). However, PEDOT:PSS has a much lower conductivity than metal materials. Single-walled carbon nanotubes (SWCNTs) have superior electrical and mechanical properties, and nanoscale size (Rathinavel et al., 2021; Dewey et al., 2024; Park et al., 2024), which make them particularly advantageous for incorporation with PEDOT:PSS, leading to significant improvements in the composite's electrical performance.

To enable synchronous neural signal detection from both the striatum and CA1 neurons, in this study we designed and fabricated two MEAs tailored to the structural characteristics of these brain regions. The electrode sites were modified with a nanocomposite material, SWCNTs/PEDOT:PSS, to improve both biocompatibility and electrical performance, facilitating high-quality electrophysiological recordings. By conducting goal-directed navigation behavior experiments on rats in a maze, we explored the encoding processes of movement initiation and spatial location perception in these two brain regions, as well as the interactions between their neural signals.

2 Results and discussion

2.1 Characterization of electrode morphology and electrical performance

The custom-made MEAs were designed according to the shape and size of the brain region and fabricated using the micro-electro-mechanical system (MEMS) process (Xu et al., 2024). The detailed fabrication process is described in the Experiment Section. Two MEAs were implanted into the brain of Sprague-Dawley rats **(Fig. 1a)**. The MEAs implanted into the striatum consisted of 4 shanks, with 8 recording sites on each shank, covering both the dorsal and ventral striatum regions. The probe implanted into the hippocampus targeted the CA1 subregion, with a total of 16 recording sites. **Fig. 1b** presents top-view microscope images of the tips of the 4-shank MEAs following modification with SWNCTs/PEDOT:PSS. **Fig. S1** illustrates the details of electrode tips implanted in the striatum and hippocampal CA1 region. The black rectangle represents the modified ground electrode, the black circle denotes the modified recording electrode, and the white circle indicates the

unmodified bare electrode site. The strip-shaped ground electrode has a much larger area than the recording electrode. This design aims to achieve common grounding between the detection equipment and biological tissues, thereby improving the stability of signal recording. The recording electrodes are placed close to the edge of the electrode, which can reduce the distance to neurons in the direction of the electrode surface and thus enhance the efficiency of signal acquisition. Meanwhile, the small gap reserved between the recording electrodes and the electrode edge can improve the structural stability of the electrode during fabrication and use, preventing damage caused by physical etching, chemical corrosion, and implantation procedures. Scanning electron microscopy images at the nanoscale demonstrate that SWCNTs and PEDOT:PSS were thoroughly mixed and firmly adhered to the surface of the detection sites (**Figs. 1c, d**). The conductive polymer PEDOT:PSS exhibited good biocompatibility along with conductivity, while SWCNTs showed superior electrical conductivity (Burnstine-Townley et al., 2020). We calculated the specific surface area of electrode sites modified with different materials based on AFM scans (Macht et al., 2011). The specific surface area of the sites increased to variable degrees after modification with PEDOT:PSS and SWCNTs/PEDOT:PSS, thereby confirming the improvement in their electrochemical performance **(Fig. S2)**.

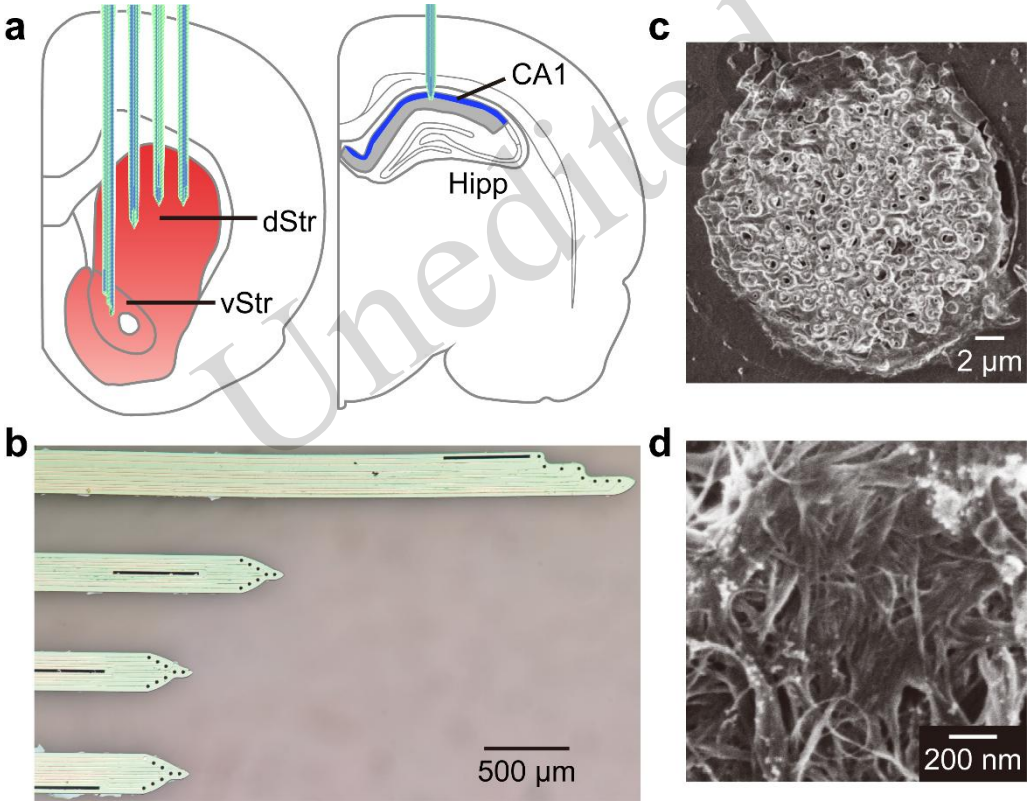

Fig. 1 Electrode implantation schematic diagram and SWCNTs/PEDOT:PSS modified MEAs. (a) Schematic diagrams of two MEAs implanted in the striatum and hippocampal CA1, respectively. CA1: Cornu Ammonis 1, Hipp: hippocampus, dStr: dorsal striatum, vStr: ventral striatum. **(b)** Microscope photographs of 4-shank MEAs after modification with SWCNTs/PEDOT:PSS. **(c-d)** Scanning electron microscopy image of the SWCNTs/PEDOT:PSS-modified microelectrode surface at the micrometer scale (c) and the nanometer scale (d).

Fig. 2a shows the impedance characteristics of unmodified and modified electrodes in the frequency range of 10 to 1,000,000 Hz. At the typical frequency of 1000 Hz, the impedance of the bare electrode was (1666.9±70.4) kΩ, while after modification with PEDOT:PSS, it was reduced to (121.2±13.1) kΩ. In comparison, the SWCNTs/PEDOT:PSS-modified electrode showed a significant reduction, with an impedance of (19.0±1.1) kΩ (n=10, mean±SEM. SEM: standard error of mean) (**Fig. 2b**). **Fig. 2c** shows that electrodes modified with SWCNTs/PEDOT:PSS had a lower phase delay than bare electrodes. The electrical conductivity of PEDOT originates from the continuous π-conjugated system formed by its molecular conjugated structure,

and PSS can enhance its conductive performance. In carbon nanotubes (CNTs), each carbon atom forms strong covalent bonds with three adjacent carbon atoms. The electrons that do not participate in hybridization can move freely within the conjugated system of the entire carbon nanotube, providing a structural basis for the electrical conductivity of the material. In addition, CNTs have an extremely high aspect ratio, which enables them to interlock with each other in the network structure formed by PEDOT:PSS, constructing an efficient three-dimensional (3D) conductive network. This network not only allows the material to form a denser microstructure (**Fig. S3**) but also further increases the specific surface area of the material, ultimately effectively improving the electrical conductivity and optimizing the conductive performance. The modified electrodes were subjected to ultrasonication (180 W) in deionized water and implanted into the rat brain, respectively, and their impedance curves were measured (**Fig. 2d**). The results showed that ultrasonication did not significantly alter the electrode impedance (**Fig. 2e**), indicating excellent stability. However, after implantation into the rat brain, the impedance at 1000 Hz increased from (19.0±1.1) kΩ to (33.6±2.1) kΩ (**Fig. 2f**). This increase is likely attributable to the adhesion of brain tissue onto the electrode surface during and after implantation, as well as interactions between the electrode site and the brain tissue environment. Despite the slight rise in impedance, the electrodes remained capable of reliable electrophysiological signal detection. Additionally, we statistically analyzed the signal-to-noise ratio (SNR) of neural signals recorded by the electrodes implanted in the rat brain for 20 days. The electrodes maintained a stable noise baseline and a good SNR over time after implantation, demonstrating the stability of the modified electrodes (**Fig. S4**).

These findings highlight the exceptional electrical performance of the SWCNTs/PEDOT:PSS-modified MEAs. The lower electrode impedance corresponds to a reduced noise baseline (Cogan et al., 2008). To further verify the biocompatibility of the MEA electrodes, we implanted MEA, microwire array, and tungsten electrodes respectively into the brain. After explantation, immunofluorescence staining was performed for astrocytes, microglia, and neurons (**Fig. S5**). The fluorescence intensities of different cell types were quantified using ImageJ (Schindelin et al., 2015) (**Fig. S6**). The results show that the number of glial cells around the MEA implantation site was significantly lower than that around the other two types of electrodes, indicating better biocompatibility and reduced tissue damage. The use of the conductive polymer PEDOT:PSS enhances the electrode's biocompatibility (Ibanez et al., 2018; Zeglio et al., 2019), facilitating improved in situ detection of electrophysiological signals.

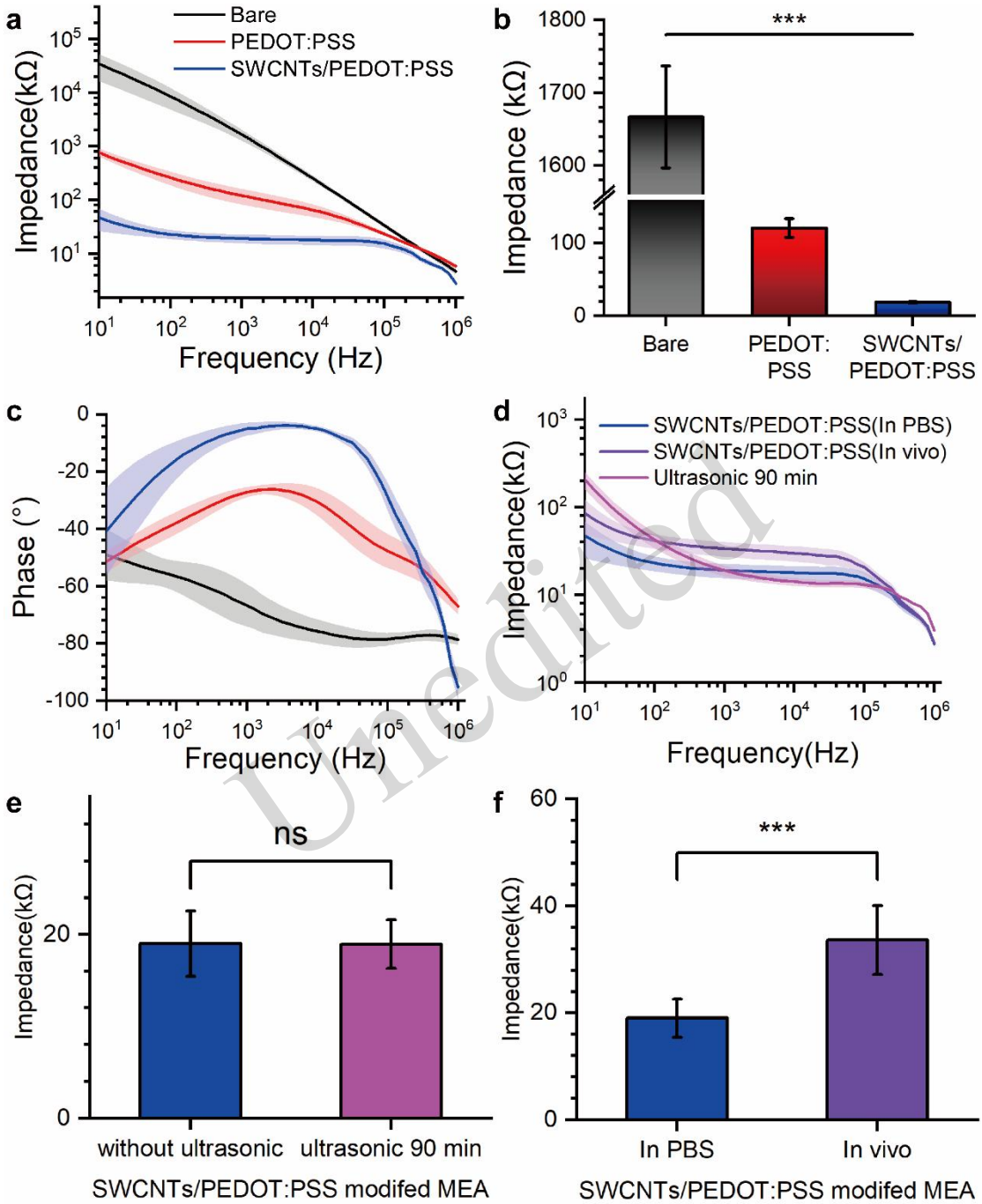

Fig. 2 Electrical characterization of microelectrode arrays (MEAs). **(a)** Impedance properties of unmodified and modified electrodes at different frequencies. **(b)** Impedance characteristics of bare electrodes and modified electrodes at 1000 Hz. **(c)** Phase delay of bare electrodes and modified electrodes among different frequencies. **(d)** Impedance curves of electrodes modified with SWCNTs/PEDOT:PSS (blue line), modified electrodes after 90 min ultrasonication (magenta), and modified electrodes implanted in a rat brain (purple). **(e)** Impedance comparison between electrodes before and after ultrasonication at 1000 Hz. **(f)** Impedance comparison between electrodes in vitro in PBS solution and electrodes in a rat brain at 1000 Hz. The data are expressed as mean±SEM, n=10, ***P<0.001, ns, not significant. SEM: Standard Error of the Mean.

2.2 Behavioral experiments and the characteristics of electrophysiological recording signals

After each rat completed training in the maze, two MEAs were implanted into its brain (**Fig. 3a**). **Fig. 3b**

illustrates the structure of the maze, which comprises a single path and two goal positions (labeled Goal 1, Goal 2). The actual path and walls are black; the colors in the figure are used for illustrative purposes. The rat starts from the red area and, upon reaching the goal position, may receive a piece of peanut as reward at the goal position. The rat's movement path is restricted to a one-way direction (**Fig. 3c**). Each time the rat starts from the red area and returns to the red area is considered one trial. The experiment was divided into three stages. In Stage 1, rewards were given only at Goal 2. In Stage 2, rewards were given at both Goal 1 and Goal 2. In Stage 3, food rewards were no longer given at Goal 1 (**Fig. 3d**). Each stage consisted of 20 to 30 trials, and transitions between stages occurred without any external cueing.

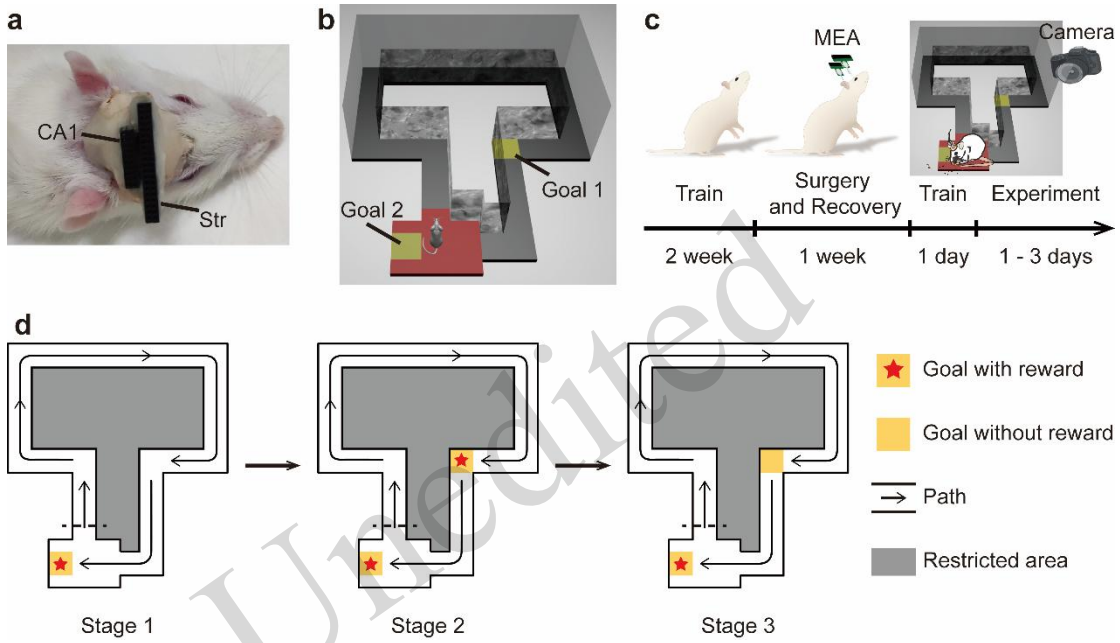

Fig. 3 Schematic diagrams of the experimental procedure and behavioral task. (a) Photographs depicting two MEAs implanted in the rat brain, with the corresponding brain regions labeled. CA1: Cornu Ammonis 1, Str: striatum. **(b)** A three-dimensional schematic diagram of the maze, with two goal positions marked. All walls are black and opaque, with some walls hidden and not depicted. **(c)** Diagram illustrating the experimental procedure. **(d)** The experimental paradigm consists consisted of three stages. The rat's movement direction is represented by black lines and arrows. The black dashed line represents the starting line of a trial.

The rat's movement trajectories in the maze are shown in **Fig. 4a**. The transition from a stationary to a moving state is highlighted by the red line. **Figs. 4b and 4c** further illustrates the changes in the linearized position and acceleration during 20 s. After movement began, the rat's position and acceleration fluctuated significantly.

Fig. 4d shows that some neurons in CA1 and vStr (Ch1 - 4) exhibited denser firing in the seconds preceding movement, while **Fig. 4e** shows more tightly packed local field potentials (LFPs) during the same period (Ch1 - 4). After movement began, the neuronal firing activity rapidly diminished, and the LFPs returned to slow oscillations. The control group (Ch7) showed firing activity (**Fig. 4d**) and LFPs (**Fig. 4e**) of a neuron in the CA region that was not related to movement events. Its firing activity was sparse over the 20 s, and the LFPs exhibited slow oscillations throughout the period. Neurons in dStr (Ch5 - 6), on the other hand, did not show this effect as prominently. This result suggests that CA1 and vStr may be involved in the process of movement initiation. Therefore, a quantitative analysis of the movement events was performed.

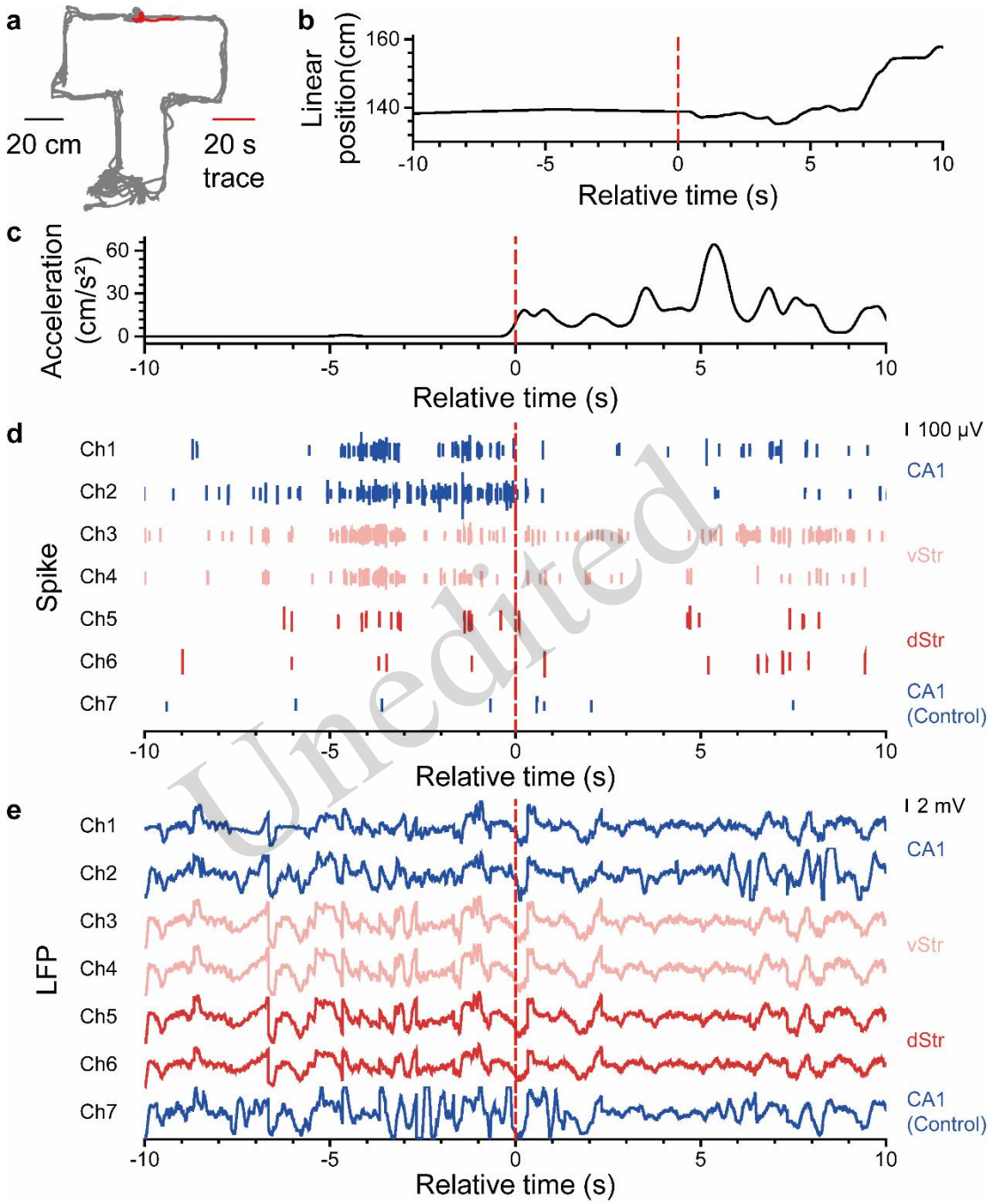

Fig. 4 Spatial Trajectories and Electrophysiological Signals. (a) The gray line represents the rat's movement trajectory, with the trajectories 20 s before and after the movement marked by the red line. **(b)** After converting 2D trajectories into linearized trajectories, the trajectories within 20 s in (a) are plotted to show the change in the linear position over time. Relative time is calculated with movement onset as time = 0. **(c)** The variation in acceleration during the 20 s. **(d)** The spike trains of neurons across different channels during the 20 s. The blue line represents neurons in CA1, the pink line represents neurons in vStr, and the red line represents neurons in dStr, with the different brain regions labeled on the right-hand side. **(e)** LFP traces across different channels during the 20 s. The red dashed line denotes the moment when the motion state changed.

2.3 vStr neurons participate in movement initiation and signal CA1 neurons

The movement onset time was identified using a threshold from the acceleration curve (see Experimental

Section), and acceleration changes were recorded for 20 s before and after the movement began, and aligned to the moment of movement onset. The average acceleration waveform is shown in **Fig. 5a**.

Peri-event time histograms (PETH) were constructed to depict neuronal firing activities during the 20-s period (**Figs. 5b-5d**). Neurons modulated by movement initiation (see Experimental Section) are shown in **Figs. 5b** (CA1) and **5c** (vStr). In the 5 s preceding movement onset, the average firing rate significantly increased across different movement initiation events and rapidly declined to baseline levels after movement began. A total of 10 neurons in CA1 and 12 neurons in vStr were identified as being modulated by movement initiation. In contrast, no neurons in the dStr were found to be modulated by movement initiation (from 3 rats). Their firing rates exhibited no significant changes over the 20 s (**Fig. 5d**). **Fig. 5e** shows that the LFPs of vStr neurons preceded those of CA1 neurons by 50 ms. Combined with spike activities, it can be inferred that movement initiation information flows from the vStr to CA1.

The involvement of the vStr in movement initiation is consistent with previous findings (Ko et al., 2016; Suzuki et al., 2020; Levcik et al., 2023). Few studies have reported a direct pathway from vStr to CA1. The information transfer between these regions is likely mediated through indirect pathways, such as projections from the vStr into the thalamus, ventral tegmental area, or prefrontal cortex, which then connect to the hippocampal CA1 region (Bueno-Junior et al., 2018; Yang et al., 2018; Douma et al., 2020).

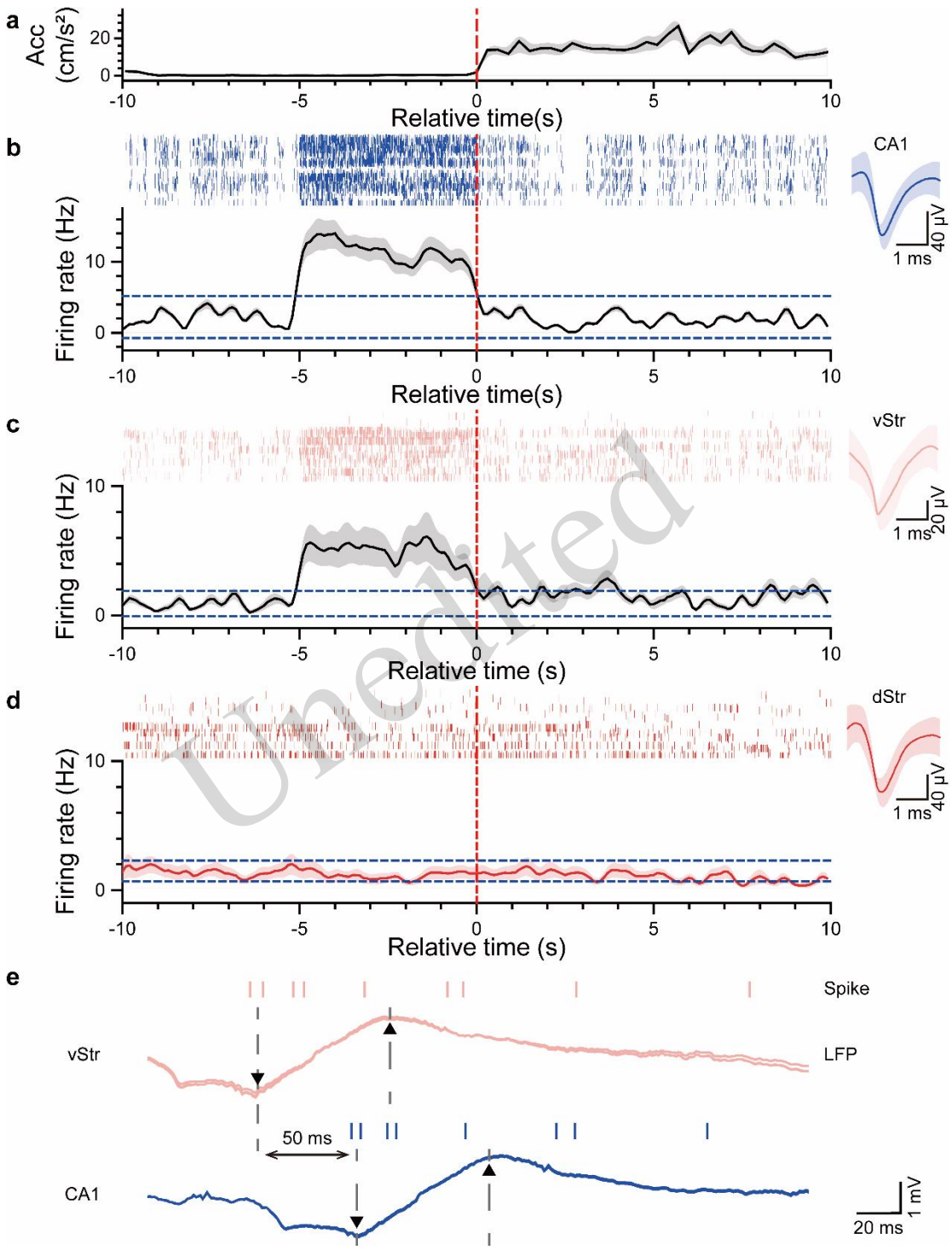

Fig. 5 Firing activities and information transmission before and after movement in CA1 and Str neurons. (a) The average acceleration curve within 20 s before and after movement onset (n = 58). The red dashed line denotes the moment of movement onset. **(b - d)** The firing activities of three neurons from CA1 (b), vStr (c), and dStr (d) during the 20 s. The upper panel shows the spike raster for different movement events. Each row represents a single movement event. The lower panel shows the mean firing rate curve. The two blue dashed lines denote the 99% confidence interval of the baseline. A significant difference in mean firing rate is indicated when the curve exceeds the blue dashed line range ($p < 0.01$). The right panel shows the spike waveform. **(e)** LFP traces from vStr (pink, n=3) and CA1 (blue, n=3) are shown, with peaks and troughs marked by triangles. The displayed LFPs are within the 5 s preceding movement onset. The spike raster is shown above the LFPs and the delay in information transmission between the two brain regions is marked.

2.4 Place fields in CA1 and place-related firing in dStr

The calculation of the position firing rate map is detailed in the Experimental Section. Note that both the traces and spikes were velocity-filtered to avoid interference from periods of immobility or stopping to consume food rewards (Duvelle et al., 2019). In the hippocampal brain region, neurons that fire collectively at a specific position or several specific positions are referred to as place cells, and the areas where they fire are called place fields. **Fig. 6a** shows a neuron with stable place fields across three stages, while **Fig. 6b** shows Cell 2, which exhibits a place field in Stage 2. **Fig. 6b** shows Cell 3, which displays the neuron place firing rate heatmap of different stages. The spatial information content (SIC) represents the amount of spatial information transmitted by each spike, and its calculation method is detailed in the Experimental Section. In CA1, the SIC of place cells across the three stages was (1.3±1.2) bits/spike (Stage 1), (3.12±1.1) bits/spike (Stage 2), and (2.3±1.6) bits/spike (Stage 3, n = 9, from 3 rats, mean±SD. SD: standard deviation). In dStr, the spatial information content of position-related cells was (0.4±0.2) bits/spike (Stage 1), (0.5±0.2) bits/spike (Stage 2), and (0.4±0.1) bits/spike (Stage 3, n = 5, from 3 rats, mean ± SD) (**Fig. S7**).

From Stage 1 to Stage 3, the spatial information content of CA1 place cells first increased and then decreased, which corresponds to the appearance and disappearance of Goal 1. This suggests that neurons in the CA1 region of the rat brain are capable of dynamically learning the changing goal position information in the external environment. Because the spatial information content of place-related cells in the dStr showed no significant changes among the three stages and the inferred direction of information transferred from CA1 to dStr in **Fig. 6c**, we speculate that the spatial information in CA1 aids dStr neurons in encoding other types of information, including rewards and habitual behaviors (Guida et al., 2022; Bech et al., 2023).

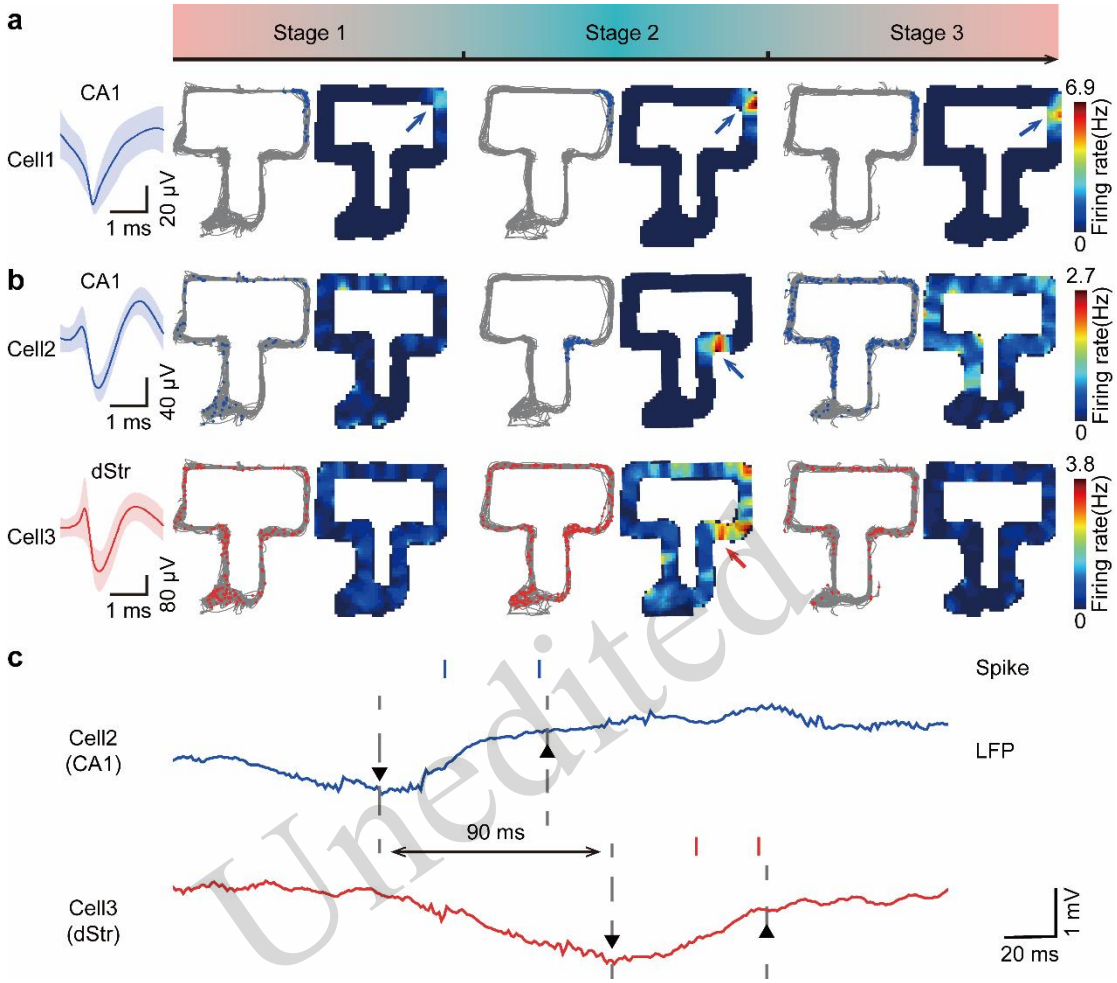

Fig. 6 The spatial firing characteristics of CA1 and dStr neurons across different stages. (a) A hippocampal cell that maintained a stable place field across all three stages. Left: Spike waveform. Middle: Trajectories (grey line) with spike positions (blue dots) and place firing rate heatmaps for each of the three stages. Right: The color bar of the heatmap, with the peak firing rate labeled at the top. The position of the place field is indicated by a blue arrow. **(b)** A hippocampal-striatal cell pair. Cell 2 in the hippocampus exhibits a place field (located near Goal 1) during Stage 2, while Cell 3 in dStr shows place-related firing at the corresponding position. The spike positions in Cell 3 are plotted as red dots. The place-related firing position is indicated by a red arrow. **(c)** The potential information transfer between Cell 2 and Cell 3. LFP traces from CA1 (blue) and dStr (red) are shown, with peaks and troughs marked by triangles. The LFPs shown correspond to the period of the place field during Stage 2. The spike raster is displayed above the LFPs.

3 Conclusions

The designed MEAs are well-suited for the striatal and hippocampal regions. After fabrication using MEMS technology, the electrodes exhibited high spatiotemporal resolution. Coating the electrode sites with SWCNTs/PEDOT:PSS nanocomposites improved their electrical properties, significantly reducing electrode impedance and phase delay, which in turn decreased electrophysiological recording noise, thereby improving the SNR.

Our preliminary data from a goal-directed navigation task in three rats suggest that neurons in the vStr may be involved in movement initiation and could potentially transmit information to CA1 via indirect pathways. Furthermore, the observed activity of CA1 place cells is consistent with a crucial role in learning new goal positions and may facilitate the transmission of spatial information to the dStr. These results provide initial evidence for a potential cross-circuit communication mechanism, which warrants validation in larger-scale studies.

Through a goal-directed navigation task in rats, we found that neurons in the vStr are involved in the initiation of movement and may transmit information to CA1 neurons via indirect pathways. Additionally, place cells in CA1 play a crucial role in learning and representing new goal positions, transmitting spatial information to neurons in the dStr.

The MEAs, modified with nanocomposites, provide an excellent platform for studying neural activity across multiple brain regions. This research lays a foundation for future studies on the functional differences and connections between the hippocampus and striatum. We aim to further explore the information transmission pathways between the hippocampus and striatum, as well as the changes in the encoding of information throughout this process.

Data availability statement

The data that support the findings of this study are available from the corresponding author upon reasonable request.

Declaration on the use of generative AI tools

No generative AI tools were used in the preparation of this manuscript.

Acknowledgments

This work was sponsored by the National Natural Science Foundation of China (No. 62121003, T2293730, T2293731, 62333020, 62171434 and 62471291), the National Key Research and Development Program of China (2022YFC2402501, 2022YFB3205602), `the Major Program of Scientific and Technical Innovation 2030 (2021ZD02016030), the Joint Foundation Program of the Chinese Academy of Sciences (No. 8091A170201), and the Scientific Instrument Developing Project of the Chinese Academy of Sciences (No. PTYQ2024BJ0009).

Author contributions

Jin SHAN and Wei XU designed the experiments, fabricated the devices, analyzed the data, and drafted the manuscript. Jinping LUO and Yaoyao LIU contributed to the study concept. Ming LI and Luyi JING assisted with the data analysis. Yu WANG, Shiya LV, and Zhaojie XU assisted with the device fabrication. Juntao LIU, Yiming DUAN, and Qianli JIA assisted with the experiments. Yilin SONG, Mixia WANG, and Xinxia CAI guided the theoretical analysis, reviewed the manuscript, and checked it for final submission. All the authors have approved the submitted version.

Compliance with ethics guidelines

Jin SHAN, Wei XU, Jinping LUO, Yaoyao LIU, Ming LI, Luyi JING, Yu WANG, Shiya LV, Zhaojie XU, Juntao LIU, Yiming DUAN, Qianli JIA, Yilin SONG, Mixia WANG, and Xinxia CAI declare that they have no conflict of interest.

All institutional and national guidelines for the care and use of laboratory animals were carried out with the permission of the Beijing Association on Laboratory Animal Care and approved by the Institutional Animal Care and Use Committee at the Aerospace Information Research Institute, Chinese Academy of Sciences (No. AIRCAS-202302-01).

References

Bech P, Crochet S, Dard R, et al., 2022. Striatal dopamine signals and reward learning. *Function*, 2023, 4(3): zqad056. https://doi.org/10.1016/j.neubiorev.2022.104826

Bettucci O, Matrone GM, Santoro F, 2022. Conductive polymer-based bioelectronic platforms toward sustainable and biointegrated devices: a journey from skin to brain across human body interfaces. *Adv Mater Technol*, 7(1): 2100293. https://doi.org/10.1002/admt.202100293

Bueno-Junior LS, Leite JP, 2018. Input convergence, synaptic plasticity and functional coupling across hippocampal-prefrontal-thalamic circuits. *Front Neural Circuits*, 2018, 12: 40. https://doi.org/10.3389/fncir.2018.00040

Burnstine-Townley A, Eshel Y, Amdursky N, 2020. Conductive scaffolds for cardiac and neuronal tissue engineering: governing factors and mechanisms. *Adv Funct Mater*, 30(2): 1901369. https://doi.org/10.1002/adfm.201901369

Cholvin T, Hainmueller T, Bartos M, 2021. The hippocampus converts dynamic entorhinal inputs into stable spatial maps. *Neuron*, 109(19): 3135–3148. https://doi.org/10.1016/j.neuron.2021.09.019

Cogan S F, 2008. Neural stimulation and recording electrodes. *Annu Rev Biomed Eng*, 10: 275–309. https://doi.org/10.1146/annurev.bioeng.10.061807.160518

Cruz KG, Leow YN, Le NM, et al., 2023. Cortical circuits for flexible sensorimotor integration. *Physiol Rev*, 103(1): 347–394. https://doi.org/10.1016/j.neuron.2021.09.019

Dewey HM, Lamb A, Budhathoki-Uprety J, 2024. Recent advances on applications of single-walled carbon nanotubes as cutting-edge optical nanosensors for biosensing technologies. *Nanoscale*, 16(30): 16344–16375. https://doi.org/10.1039/D4NR01892C

Donahue MJ, Sanchez-Sanchez A, Inal S, et al., 2020. Tailoring PEDOT properties for applications in bioelectronics. *Mater Sci Eng R Rep*, 140: 100546. https://doi.org/10.1016/j.mser.2020.100546

Douma EH, de Kloet ER, 2020. Stress-induced plasticity and functioning of ventral tegmental dopamine neurons. *Neurosci Biobehav Rev*, 108: 48–77. https://doi.org/10.1016/j.neubiorev.2019.10.015

Dupret D, O'Neill J, Pleydell-Bouverie B, et al., 2010. The reorganization and reactivation of hippocampal maps predict spatial memory performance. *Nat Neurosci*, 13(8): 995–1002. https://doi.org/10.1038/nn.2599

Duvelle É, Grieves RM, Hok V, et al., 2019. Insensitivity of place cells to the value of spatial goals in a two-choice flexible navigation task. *J Neurosci*, 39(13): 2522–2541. https://doi.org/10.1523/JNEUROSCI.1578-18.2018.

Guida P, Michiels M, Redgrave P, et al., 2022. An fMRI meta-analysis of the role of the striatum in everyday-life vs laboratory-developed habits. *Neurosci Biobehav Rev*, 141: 104826. https://doi.org/10.1016/j.neubiorev.2022.104826

Huang Y, Tang L, Jiang Y, 2024. Chemical strategies of tailoring PEDOT:PSS for bioelectronic applications: synthesis, processing and device fabrication. *CCS Chem*, 6(12): 1844–1859. https://doi.org/10.31635/ccschem.024.202403858

Ibanez JG, Rincón ME, Gutierrez-Granados S, et al., 2018. Conducting Polymers in the Fields of Energy, Environmental Remediation, and Chemical-Chiral Sensors. *Chem Rev*, 2018, 118(9): 4731–4816. https://doi.org/10.1021/acs.chemrev.7b00482

Kayser LV, Lipomi DJ, 2019. Stretchable conductive polymers and composites based on PEDOT and PEDOT:PSS. *Adv Mater*, 31(10): 1806133. https://doi.org/10.1002/adma.201806133

Ko D, Wanat M J. Phasic dopamine transmission reflects initiation vigor and exerted effort in an action- and region-specific manner. *J Neurosci*, 2016, 36(7): 2202–2211. https://doi.org/10.1523/JNEUROSCI.1279-15.2016

Lee D, Moon HC, Tran BT, et al., 2018. Characterization of tetrodes coated with Au nanoparticles (AuNPs) and PEDOT and their application to thalamic neural signal detection in vivo. *Exp Neurobiol*, 27(6): 593–603. https://doi.org/10.5607/en.2018.27.6.593

Levcik D, Sugi AH, Aguilar-Rivera M, et al., 2023. Nucleus accumbens shell neurons encode the kinematics of reward approach locomotion. *Neuroscience*, 524: 181–196. https://doi.org/10.1016/j.neuroscience.2023.06.002

Macht F, Eusterhues K, Pronk GJ, et al., 2011. Specific surface area of clay minerals: comparison between atomic force microscopy measurements and bulk-gas (N_2) and -liquid (EGME) adsorption methods. *Appl Clay Sci*, 53(1): 20–26. https://doi.org/10.1016/j.clay.2011.04.006

Marks WD, Yamamoto N, Kitamura T, et al., 2021. Complementary roles of differential medial entorhinal cortex inputs to the hippocampus for the formation and integration of temporal and contextual memory. *Eur J Neurosci*, 54(8): 6762–6779. https://doi.org/10.1111/ejn.14737

Park S, Song Y, Ryu B, et al., 2024. Highly conductive ink based on self-aligned single-walled carbon nanotubes through inter-fiber sliding in cellulose fibril networks. *Adv Sci*, 11(8): 2402854. https://doi.org/10.1002/advs.202402854

Penner MR, Mizumori SJY, 2012. Neural systems analysis of decision making during goal-directed navigation. *Prog Neurobiol*, 96(1): 96–135. https://doi.org/10.1016/j.pneurobio.2011.08.010

Rathinavel S, Priyadharshini K, Panda D, 2021. A review on carbon nanotube: An overview of synthesis, properties, functionalization, characterization, and the application. *Mater Sci Eng B*, 268: 115095. https://doi.org/10.1016/j.mseb.2021.115095

Schindelin J, Rueden C T, Hiner M C, et al., 2015. The ImageJ ecosystem: an open platform for biomedical image analysis. *Mol Reprod Dev*, 82(7-8): 518–529. https://doi.org/10.1002/mrd.22489

Sosa M, Giocomo LM. Navigating for reward. *Nat Rev Neurosci*, 2021, 22(8): 472–487.
https://doi.org/10.1038/s41583-021-00479-z

Suzuki S, Lawlor VM, Cooper JA, et al., 2021. Distinct regions of the striatum underlying effort, movement initiation and effort discounting. *Nat Hum Behav*, 5(3): 378–388.
https://doi.org/10.1038/s41562-020-00972-y

Syed ECJ, Grima LL, Magill PJ, et al., 2016. Action initiation shapes mesolimbic dopamine encoding of future rewards. *Nat Neurosci*, 19(1): 34–36.
https://doi.org/10.1038/nn.4187

Tryon VL, Penner MR, Heide SW, et al., 2017. Hippocampal neural activity reflects the economy of choices during learned decision making. *Hippocampus*, 27(7): 743–758.
https://doi.org/10.1002/hipo.22720

Xu W, Wang M, Yang G, et al., 2024. Neuronal activity in the ventral tegmental area during goal-directed navigation recorded by low-curvature microelectrode arrays. *Microsyst Nanoeng*, 10(1): 145.
https://doi.org/10.1038/s41378-024-00778-2

Yang H, de Jong JW, Tak Y, et al., 2018. Nucleus accumbens subnuclei regulate motivated behavior via direct and indirect pathways. Neuron, 97(2): 434–449.
https://doi.org/10.1016/j.neuron.2017.12.022

Zhang S, Song Y, Wang M, et al., 2016. A silicon based implantable microelectrode array for electrophysiological and dopamine recording from cortex to striatum in the non-human primate brain. *Biosens Bioelectron*, 85: 53–61.
https://doi.org/10.1016/j.bios.2016.04.087

Zeglio E, Rutz A L, Winkler T E, et al., 2019. Conjugated polymers for assessing and controlling biological functions. *Adv Mater*, 31(22): e1806712.
https://doi.org/10.1002/adma.201806712

Supplementary information

Figs. S1-S9; Materials and methods